



Effect of nickel content on structural, morphological and magnetic properties of $\text{Ni}_x\text{Co}_{1-x}\text{Fe}_2\text{O}_4/\text{SiO}_2$ nanocomposites

Thomas Dippong^{a, *}, Erika Andrea Levei^b, Oana Cadar^b, Iosif Grigore Deac^c,
Lucian Diamandescu^d, Lucian Barbu-Tudoran^e

^a Technical University of Cluj-Napoca, North University Center of Baia Mare, Department of Chemistry and Biology, 76 Victoriei Street, 430122, Baia Mare, Romania

^b INCDO-INOE 2000, Research Institute for Analytical Instrumentation, 67 Donath Street, 400293, Cluj-Napoca, Romania

^c Babes-Bolyai University, Faculty of Physics, 1 Kogalniceanu Street, 400084, Cluj-Napoca, Romania

^d National Institute of Materials Physics, 405A Atomistilor Street, 077125, Magurele, Romania

^e National Institute for Research and Development of Isotopic and Molecular Technologies, 67-103, Donath Street, 400293 Cluj-Napoca, Romania



ARTICLE INFO

Article history:

Received 22 November 2018

Received in revised form

27 January 2019

Accepted 29 January 2019

Available online 30 January 2019

Keywords:

Nanocomposite
Nickel-cobalt ferrite
Crystallinity degree
Magnetic properties
Mössbauer effect

ABSTRACT

$\text{Ni}_x\text{Co}_{1-x}\text{Fe}_2\text{O}_4/\text{SiO}_2$ nanocomposites ($x = 0, 0.25, 0.50, 0.75$ and 1.00) were synthesized by a modified sol-gel method. The X-ray diffraction (XRD) patterns revealed the crystalline phases and the crystallite size variation with increasing annealing temperature and Ni content. The lattice constants, cell volume, X-ray density, hopping length in A and B sites, average crystallites size and relative crystallinity calculated from XRD data are consistent with the mixed spinel structure. The transmission electron microscopy images reveal the spherical shape of nanoparticles and their size increase with increasing annealing temperature. The magnetic properties such as saturation magnetization (M_s), remanent magnetization (M_r), coercivity (H_c), magnetic moments per unit cell (n_B) and anisotropy (K) decrease with increasing Ni content, but they increase with the annealing temperature due to the influence of the cation stoichiometry and their specific sites occupancy. The Mössbauer spectra showed the characteristic magnetic patterns of Co and Ni spinels and revealed only the presence of Fe^{3+} . The Ni-rich nanocomposites presented superparamagnetic behavior, while the Ni-poor nanocomposites ferromagnetic behavior.

© 2019 Elsevier B.V. All rights reserved.

1. Introduction

The production of high quality ferrites remains a challenge. The properties of these materials are dependent upon microstructure and composition, and they are sensitive towards the processing techniques [1]. NiFe_2O_4 and CoFe_2O_4 are attractive materials for numerous applications such as microwave devices, recording media, computer memory cores, gas sensors, high density information storage, drug delivery, low energy inductors, medical instruments, telecommunication, catalysts, high frequency transformers, microwave and dye absorbers [1–5]. A wide range of methods were used to synthesize NiFe_2O_4 and CoFe_2O_4 nanoparticles, such as sol-gel, solid-state reaction, microwave-assisted flash combustion technique, high energy ball milling, hydrothermal, chemical coprecipitation, autocombustion, spray pyrolysis, matrix isolation,

forced hydrolysis, laser-induced vapor phase reactions and solid state evaporation condensation [1–10]. Among these methods, the sol-gel is considered a simple, low-cost, highly reproducible method that allows excellent composition control while it requires low processing time and low energy consumption [3].

The spinel structure of Co–Ni ferrites consists of a cubic close-packed lattice of 32 oxygen atoms with the metal ions distributed in two different sub-lattices: 8 tetrahedral Ni^{2+} or Co^{2+} (A-sites) and 16 octahedral Fe^{3+} (B-sites) [2,4,9,10]. The inverse spinel structure is characterized by 8 Ni^{2+} or Co^{2+} and 8 Fe^{3+} cations occupying half of the octahedral sites and 8 Fe^{3+} ions occupying tetrahedral sites [4]. In the mixed spinel structure, the number of Fe^{3+} ions in octahedral sites increase, while that of the Fe^{3+} ions in tetrahedral sites decrease due to presence of divalent ions (Ni^{2+} , Co^{2+}) in tetrahedral sites [4].

Polycrystalline CoFe_2O_4 is a hard magnetic material having high coercivity (H_c), high chemical stability, good electrical insulation, large mechanical hardness and rather high saturation magnetization (M_s , 80.0 emu/g) at room temperature [2]. By replacing Ni^{2+}

* Corresponding author.

E-mail address: dippong.thomas@yahoo.ro (T. Dippong).

with Co^{2+} in the structure of NiFe_2O_4 , H_c and M_s increase due to higher magnetocrystalline anisotropy and higher magnetic moment of Co^{2+} . The magnetization of Co–Ni ferrites is strongly dependent on the cations distribution (Fe^{3+} , Ni^{2+} , Co^{2+}) between tetrahedral and octahedral sites. Moreover, Ni–Co ferrite exhibits high resistivity in addition to excellent magnetic properties [3]. The frequency of operation of spinel ferrites is directly proportional to square of M_s and electrical resistivity and it is inversely proportional to grain size [11]. Bulk $\text{Co}_x\text{Ni}_{1-x}\text{Fe}_2\text{O}_4$ produced by standard ceramic process showed lower resistivity with increasing Co content and semiconducting properties [12].

Previous studies demonstrated that embedded Ni–Co ferrites exhibit high magnetocrystalline anisotropy, unique magnetic structure and high correlation between the coercivity, crystallite sizes and sample preparation pressure [13]. Moreover, the increase of Ni content in $\text{Ni}_x\text{Co}_{1-x}\text{Fe}_2\text{O}_4$ determines an increase of the magnetic hyperfine fields, indicating strong superexchange interactions [12]. These findings further motivated research on the improvement of structural and magnetic properties of ferrites by cation substitution [14–16]. Our study presents the sol-gel synthesis of $\text{Ni}_x\text{Co}_{1-x}\text{Fe}_2\text{O}_4/\text{SiO}_2$ nanocomposites (NCs) and the evolution of their structural, morphological and magnetic properties with the thermal treatment at 500, 800 and 1100 °C. Also, the influence of Ni content on the structural and magnetic properties of $\text{Ni}_x\text{Co}_{1-x}\text{Fe}_2\text{O}_4/\text{SiO}_2$ NCs is discussed.

2. Experimental

2.1. Reagents

Nonahydrate ferric nitrate ($\text{Fe}(\text{NO}_3)_3 \cdot 9\text{H}_2\text{O}$) of 98% purity, hexahydrate cobalt nitrate ($\text{Co}(\text{NO}_3)_2 \cdot 6\text{H}_2\text{O}$) of 98% purity, hexahydrate nickel nitrate ($\text{Ni}(\text{NO}_3)_2 \cdot 6\text{H}_2\text{O}$) of 99% purity, 1,4-butanediol (1,4BD) of 99% purity, tetraethylorthosilicate (TEOS) of 99% purity, ethanol of 96% purity and HNO_3 65% were purchased from Merck (Germany). All reagents were used as received without further purification.

2.2. Synthesis

$\text{Ni}_x\text{Co}_{1-x}\text{Fe}_2\text{O}_4/\text{SiO}_2$ NCs were prepared by a modified sol-gel route using the following Ni/Co molar ratios: 0/1 ($x=0$), 0.25/0.75 ($x=0.25$), 0.50/0.50 ($x=0.5$), 0.75/0.25 ($x=0.75$) and 1/0 ($x=1$). The sols were prepared by mixing $\text{Fe}(\text{NO}_3)_3 \cdot 9\text{H}_2\text{O}$, $\text{Co}(\text{NO}_3)_2 \cdot 6\text{H}_2\text{O}$ and $\text{Ni}(\text{NO}_3)_2 \cdot 6\text{H}_2\text{O}$ with 1,4-BD, TEOS, ethanol and HNO_3 . In all cases, a molar ratio of 1:1:1 NO_3^- :1,4-BD:TEOS was used. The resulted sols were mixed together under continuous stirring, for 30 min, and kept at room temperature until gelation. The obtained samples were grinded, annealed at 500 °C for 4 h and at 800 and 1100 °C for 5 h, as high purity gels with high crystallites size are obtained using a thermal pretreatment before annealing.

2.3. Characterization

The Ni/Co/Fe ratio in the $\text{Ni}_x\text{Co}_{1-x}\text{Fe}_2\text{O}_4/\text{SiO}_2$ NCs was confirmed by inductively coupled plasma optical emission spectrometry (ICP-OES) using a Perkin Elmer 5300 Optima DV spectrometer, after microwave digestion with aqua regia. The formation of crystalline phases, the crystallite size, relative crystallinity, lattice constant, cell unit volume and X-ray density were investigated by X-ray diffraction (XRD) using a Bruker D8 Advance diffractometer, operating at 40 kV and 40 mA, with CuK_α radiation ($\lambda = 1.5406 \text{ \AA}$) at room temperature, while the structure and composition of the NCs by Fourier-transform infrared spectroscopy (FT-IR) using a Perkin Elmer Spectrum BX II FT-IR spectrometer. The shape and size of

Ni–Co ferrite nanoparticles embedded in SiO_2 matrix were investigated by transmission electron microscopy (TEM) using a Hitachi SU8230 ultra-high resolution scanning electron microscope, on sputter-coated samples, coupled with an Oxford Instruments X-Max 1160 EDX detector. The magnetic properties as a function of Ni-content variation in NCs were studied using a vibrating sample magnetometer (VSM) using a Cryogenic Ltd. 12 T VSM. The hysteresis loops were recorded in magnetic fields from -1 to 1 T, at room temperature. Magnetization (M) vs. magnetic field (H) measurements were performed to find the saturation magnetization M_s , up to 7 T. The powder samples were embedded in an epoxy resin to prevent any nanoparticles movement [17]. The Mössbauer spectroscopy was used to investigate the cation distribution and to establish the stoichiometry of $\text{Ni}_x\text{Co}_{1-x}\text{Fe}_2\text{O}_4$ structure. The Mössbauer measurements were performed at room temperature using a WissEL-ICE Oxford Mössbauer cryomagnetic system. The γ -rays were provided by a 10 mCi ^{57}Co source in Rh matrix. The isomer shift is given relative to α -Fe at room temperature.

3. Results and discussion

3.1. XRD analysis

The XRD patterns of NCs reveals the effect of Ni content on the $\text{Ni}_x\text{Co}_{1-x}\text{Fe}_2\text{O}_4$ ($x = 0, 0.25, 0.50, 0.75, 1$) system embedded in SiO_2 matrix (Fig. 1). In the case of samples annealed at 500 °C, for NCs without Ni ($x = 0$), well-crystallized CoFe_2O_4 (JCPDS card 22–1086) and Co_3O_4 (JCPDS file 42–1467) phases are observed [18]. For NCs containing Ni, a decrease of the intensity and a flattening of diffraction lines with the increase of Ni content are evidenced. At $x = 0.25$, poorly crystallized Co_3O_4 and $\text{Ni}_{0.25}\text{Co}_{0.75}\text{Fe}_2\text{O}_4$, while in the case of $x = 0.50$ single-phase $\text{Ni}_{0.5}\text{Co}_{0.5}\text{Fe}_2\text{O}_4$ are observed. Two phases: $\text{Ni}_{0.75}\text{Co}_{0.25}\text{Fe}_2\text{O}_4$, and NiO (JCPDS card 47–1049) are observed for $x = 0.75$, while for $x = 1$, the NiFe_2O_4 (JCPDS card 89–4927) main phase appears contaminated by NiO [18]. The formation of NiO is possible due to the presence of oxygen that cause the formation of intermediate products (NiO) instead of ferrites or due to the broken oxygen bonds on the surface, which causes incomplete exchange bonds [19].

For the samples annealed at 800 °C, the XRD patterns of NCs are more intense and better separated. A mixture of CoFe_2O_4 and Co_3O_4 for $x = 0$, $\text{Ni}_{0.25}\text{Co}_{0.75}\text{Fe}_2\text{O}_4$ and Co_3O_4 for $x = 0.25$, $\text{Ni}_{0.5}\text{Co}_{0.5}\text{Fe}_2\text{O}_4$ for $x = 0.50$, $\text{Ni}_{0.75}\text{Co}_{0.25}\text{Fe}_2\text{O}_4$ for $x = 0.75$, and NiFe_2O_4 for $x = 1$ were identified. The strong, intense and sharp reflection peaks at 1100 °C, confirm the high degree of crystallinity of CoFe_2O_4 ($x = 0$) and NiFe_2O_4 ($x = 1$) (cubic spinel structure with Fd-3m space group) [19]. For the samples annealed at 1100 °C, single phases $\text{Ni}_{0.25}\text{Co}_{0.75}\text{Fe}_2\text{O}_4$ ($x = 0.25$), $\text{Ni}_{0.5}\text{Co}_{0.5}\text{Fe}_2\text{O}_4$ ($x = 0.50$) and $\text{Ni}_{0.75}\text{Co}_{0.25}\text{Fe}_2\text{O}_4$ ($x = 0.75$) were identified. The diffraction lines of CoFe_2O_4 overlap to those of NiFe_2O_4 (isostructural compounds) [18]. For NCs with $x = 1$, the formation of NiFe_2O_4 crystalline phase is the result of low oxidation capacity, low melting point, high electronegativity, high thermal expansion coefficient and high specific heat capacity of Ni [20]. A decrease of diffraction lines intensity with the increase of Ni content was also remarked [3]. The XRD data indicated single-phase cubic NiFe_2O_4 spinel ($x = 1$) and single-phase cubic CoFe_2O_4 spinel ($x = 0$). The degree of crystallinity is given by the ratio between the sum of diffraction peaks area and the diffraction halos area. As the diffraction areas and diffraction halos are approximately constant for a particular material with the same type of scattering atoms, the degree of crystallinity can be determined also by the ratio between the sum of the diffraction areas for the sample to be analyzed and the sum of the same diffraction peaks area for a sample with 100% crystallinity. Since even in the sample with the highest crystallinity (NCs annealed at

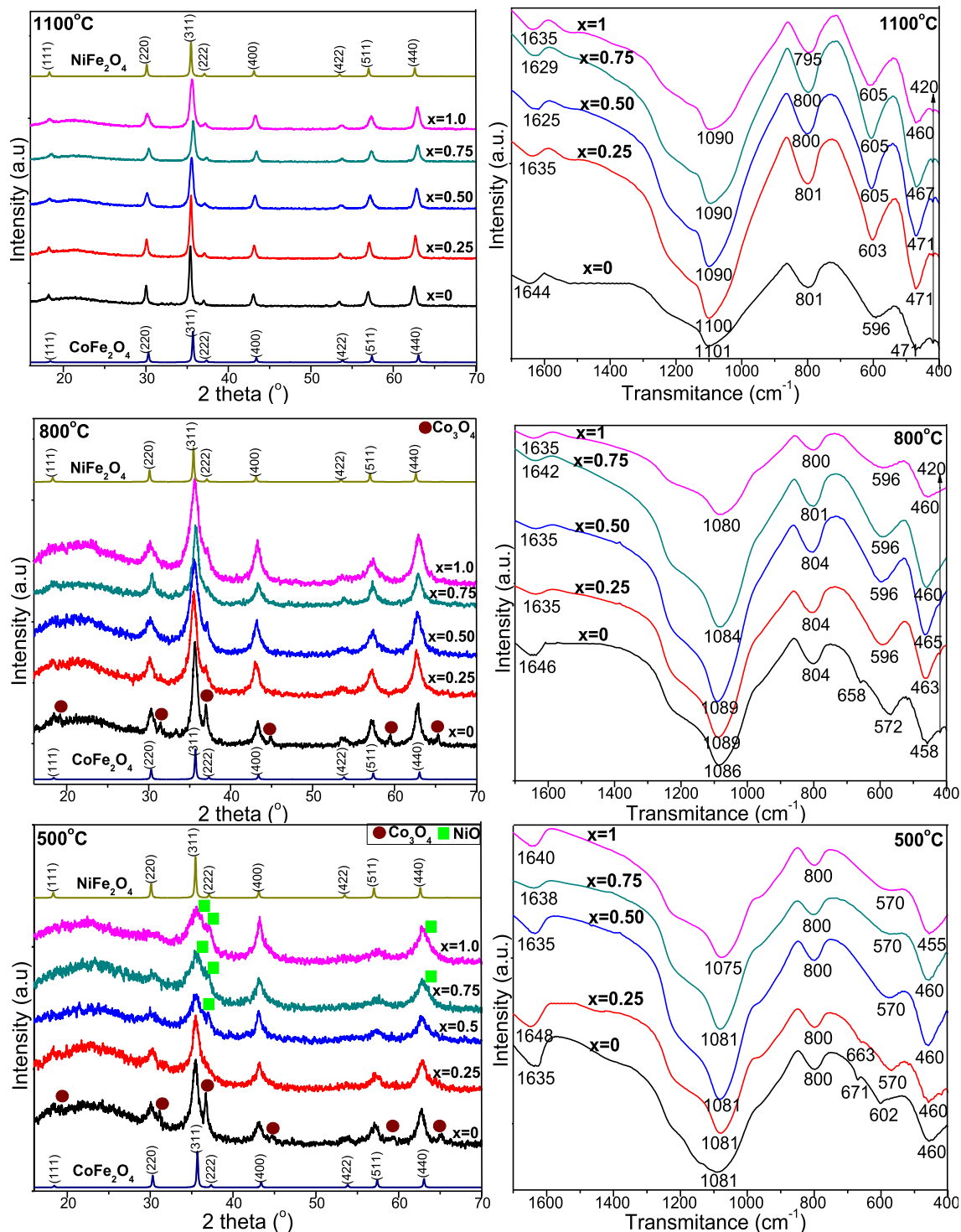


Fig. 1. XRD patterns and FT-IR spectra of $\text{Ni}_x\text{Co}_{1-x}\text{Fe}_2\text{O}_4/\text{SiO}_2$ NCs annealed at 500, 800 and 1100 °C and XRD patterns of NiFe_2O_4 (JCPDS card 89–4927) and CoFe_2O_4 (JCPDS card 22–1086).

1100 °C) amorphous phases are still observed, the crystallinity was expressed in arbitrary units (a.u.) instead of percentages. The relative crystallinity values increase with increasing Ni content. A possible explanation is the high number of small size crystallites for NCs with high Ni content and high number of big-size crystallites for NCs with low Ni content, respectively [21].

Ni^{2+} and Co^{2+} ions prefer octahedral sites, while Fe^{3+} ions occupy both octahedral and tetrahedral sites. Therefore, the

increase of Ni^{2+} content forces the Fe^{3+} ions to occupy tetrahedral sites [21]. All NCs exhibit a poly-oriented structure and the main diffraction peaks can be identified as to the planes (hkl) of (1 1 1), (2 2 0), (3 1 1-maximum intensity), (2 2 2), (4 0 0), (5 1 1) and (4 4 0), confirming the formation of a cubic structure (fcc). In case of $\text{Ni}_x\text{Co}_{1-x}\text{Fe}_2\text{O}_4$ annealed at 1100 °C, highly crystalline Ni–Co ferrite phase was observed. The peaks become sharpen and the intensity of diffraction peaks increases with increasing annealing

temperature due to enhanced crystallization degree. According to Bragg law, the increase of d-spacing in crystal structure is associated with moving θ towards lower diffraction angles [8]. For all NCs, the XRD peaks for the samples annealed at 1100 °C are shifted to lower angles, indicating the substitution of Co with Ni in the spinel structure and increasing plane distances [10]. The intensities of (2 2 0), (3 1 1) and (4 4 0) planes are more sensitive to cations in tetrahedral and octahedral sites and decrease in response to higher Ni content, due to the migration of Fe^{3+} ions from octahedral to tetrahedral sites, as Co^{2+} ions are replaced by Ni^{2+} ions [22,23].

The average crystallites size (D_{hkl}) was calculated using the Scherrer equation (Eq. (1)) [22].

$$D_{hkl} = \frac{0.9 \cdot \lambda}{\beta \cdot \cos \theta} \quad (1)$$

where λ is the wavelength of CuK_α radiation (1.5406 Å), β is the broadening of full width at half the maximum intensity (FWHM), hkl are the Miller indices, θ is the Bragg angle ($^\circ$).

The lattice constant, a (Å) was calculated from Bragg's law with Nelson-Riley correction (Eq. (2)).

$$a = \frac{\lambda \sqrt{h^2 + k^2 + l^2}}{2 \cdot \sin \theta} \quad (2)$$

where λ is the wavelength of CuK_α radiation (1.5406 Å), hkl are the Miller indices, θ is the Bragg angle ($^\circ$).

The Ni/Co/Fe molar ratio, average size of nanocrystallites (XRD) and relative crystallinity (XRD) of Ni–Co nanoparticles are presented in Table 1. The average crystallite size of Co–Ni ferrites annealed at 1100 °C is 18.2–31.7 nm, which is small enough to achieve suitable signal-to-noise ratio recommended for high density recording media [3]. This effect is due to the replacement of Co^{2+} ions in CoFe_2O_4 on the grain boundary during crystallization, leading to the reduction of grain size and favoring the formation of new nuclei and preventing further growth of grains [10]. The ICP-OES measured values show good agreement with the theoretical values.

The unit cell volume, V (Å^3) and X-ray density, d_x (g/cm^3) which reflects the packing of atoms in a unit cell, were calculated from XRD spectra using the molar mass of ferrite and Avogadro's number ($6.022 \cdot 10^{23} \text{ mol}^{-1}$) according to Eqs. (3) and (4) [2,8]. The distance between magnetic ions (d , hopping length) in A (tetrahedral) and B (octahedral) sites of NCs annealed at 800 and 1100 °C were calculated using Eqs. (5) and (6).

$$V = a^3 \quad (3)$$

$$d_x = \frac{Z \cdot M}{N_A \cdot a^3} \quad (4)$$

$$d_A = 0.25 \cdot a\sqrt{3} \quad (5)$$

$$d_B = 0.25 \cdot a\sqrt{2} \quad (6)$$

where a is the lattice constant (Å), Z is the number of molecules per unit cell (8), M is the molecular weight (g/mol) and N_A is the Avogadro number.

Table 2 shows that for samples annealed at 1100 °C, the substitution of Co^{2+} by Ni^{2+} leads to the gradually decrease of the lattice constant from 8.4379 to 8.3178 Å. This variation indicates that the Ni–Co ferrite system follows the Vegard's law. A possible explanation could be the larger ionic radius of Co^{2+} (0.740 Å) compared to that of Ni^{2+} (0.695 Å). Thus, the replacement of Co by Ni ions in the octahedral sites leads to a decrease of the lattice constant and formation of a compositionally homogeneous solid solution [3,24,25]. The change of lattice constant causes internal stress and suppresses additional grain growth during annealing [9]. The difference between theoretical and experimental values can be attributed to the approximation which considers all ions as rigid spheres distributed in a rigid manner [3].

For the samples annealed at 800 and 1100 °C, the X-ray density increases, while the lattice constant decreases with the increase of Ni content [7]. The fluctuation of XRD density caused by small fluctuations in lattice constant is probably due to the changes in the distribution of cations within A and B-sites [12]. The decrease of unit cell volume is expected with the introduction of smaller-sized Ni in the crystal lattice [3]. There is no significant difference in molecular weight of different NCs, hence the decreased unit cell volume with increased Ni content has resulted in increase of X-ray density [3].

The distance between magnetic ions (d , hopping length) in A (tetrahedral) and B site (octahedral) of NCs shows an increasing trend with the increase of Co content, attributed to higher ionic radius of Co^{2+} in comparison to Ni^{2+} . Furthermore, Co and Ni have very low, but not zero tendency for A-site occupancy, while Fe is not equally divided between A and B-sites, its value varying with Ni content [3].

Thus, for CoFe_2O_4 , an increase of crystallites size, relative crystallinity, lattice constant, unit cell volume and hopping length in A and B sites and a decrease of X-ray density at higher annealing temperatures are observed. For Ni-rich NCs, an increase of the crystallites size, relative crystallinity, X-ray density and a decrease of lattice constant, unit cell volume and hopping length in A and B sites at higher annealing temperature is remarked.

3.2. Fourier-transformed infrared spectroscopy

The FT-IR spectra of $\text{Ni}_x\text{Co}_{1-x}\text{Fe}_2\text{O}_4$ (Fig. 1) confirm the formation of the oxidic phases identified by XRD and the formation of silica matrix. The bands at 420 cm^{-1} , present only at 800 and 1100 °C, are attributed to octahedral-metal stretching vibration of Ni–O and Co–O bonds. The bands at 455–471 and $570\text{--}605 \text{ cm}^{-1}$ are attributed to intrinsic stretching vibrations of Fe–O bond and suggest the spinel formation with Fe in both octahedral and tetrahedral sites [10]. Both octahedral and tetrahedral characteristic bands shift

Table 1
Ni/Co/Fe molar ratio, average crystallites size (D_{hkl}) and relative crystallinity (RC) of $\text{Ni}_x\text{Co}_{1-x}\text{Fe}_2\text{O}_4$ annealed at 500, 800 and 1100 °C.

x	Ni/Co/Fe			D_{hkl} (nm)			RC (a.u.)		
	500	800	1100	500	800	1100	500	800	1100
0.00	0/1/2	0/1.10/1.90	0/1.01/2	10.8	12.1	31.7	20.3	51.2	81.6
0.25	0.23/0.78/2	0.25/0.75/2	0.27/0.73/2	9.8	11.5	28.1	26.7	56.0	85.2
0.50	0.54/0.46/2	0.51/0.49/2	0.48/0.52/2	7.5	10.1	24.7	32.5	61.7	89.1
0.75	0.76/0.24/2	0.77/0.23/2	0.74/0.26/2	6.2	8.1	21.4	36.9	67.5	93.2
1.00	0.98/0/2.02	1.04/0/1.96	1.10/0/2	5.1	7.2	18.2	42.4	72.8	100

Table 2
Lattice constant (a), cell volume (V), X-ray density (d_x), hopping length in A (d_A) and B (d_B) sites of $Ni_xCo_{1-x}Fe_2O_4$ annealed at 800 and 1100 °C.

x	a (Å)		V (Å ³)		d_x (g/cm ³)		dA (Å)		dB (Å)	
	800	1100	800	1100	800	1100	800	1100	800	1100
0.00	8.3551	8.4379	583.3	600.8	5.344	5.188	3.618	3.654	2.954	2.983
0.25	8.3818	8.4063	588.9	594.0	5.292	5.246	3.629	3.640	2.963	2.972
0.50	8.3710	8.3754	586.6	587.5	5.311	5.303	3.625	3.627	2.960	2.961
0.75	8.3610	8.3459	584.5	581.3	5.329	5.358	3.620	3.614	2.956	2.951
1.00	8.3522	8.3178	582.6	575.5	5.344	5.411	3.617	3.602	2.953	2.941

toward higher wavenumbers with the decrease of Ni^{2+} substitution in $CoFe_2O_4$, because the atomic weight is inverse proportional to the wavenumber in FT-IR spectra. Another explanation could be the larger ionic radius of Co^{2+} comparing to Ni^{2+} that results in larger distance of Fe–O bond [10]. In case of samples with high Co content ($x=0, 0.25$), at low temperatures, the band at $658\text{--}671\text{ cm}^{-1}$ is attributed to Co_3O_4 . The disappearance of this bands at higher temperatures (1100 °C) indicate that Co_3O_4 is reduced to CoO and then converted to ferrite [2,4,24,26]. The specific bands of SiO_2 found at $1627\text{--}1643\text{ cm}^{-1}$, are attributed to the bending vibration of the H–O–H bond, while those from $1072\text{ to }1098\text{ cm}^{-1}$, are assigned to the stretching vibration of Si–O–Si bonds [22,26,27]. The band around 800 cm^{-1} is attributed to the symmetric stretching and bending vibration of Si–O–Si chains and indicates a low degree of polycondensation in the SiO_2 network [2,4,26,27].

3.3. Mössbauer spectroscopy

The room temperature Mössbauer spectra of $Ni_xCo_{1-x}Fe_2O_4$ NCs consist in hyperfine magnetic patterns accompanied by small quadruple doublets (Fig. 2). In the hypothesis of a Lorentzian line

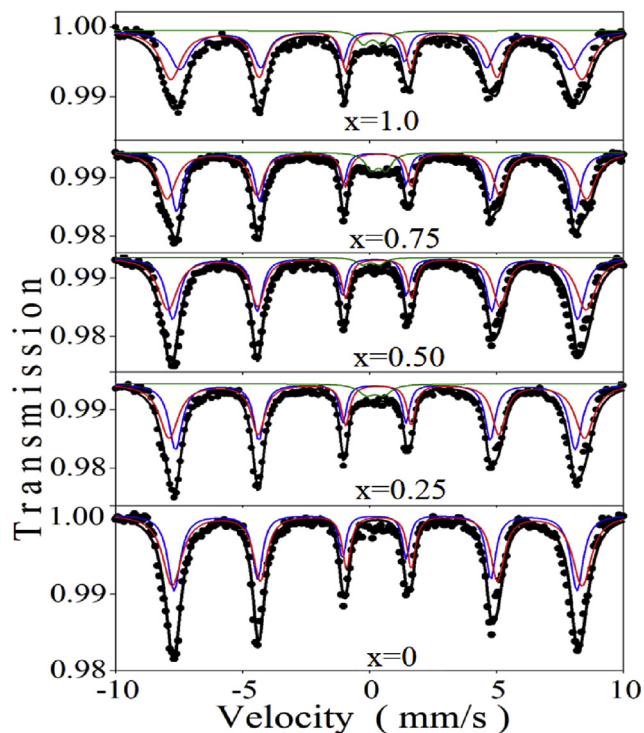


Fig. 2. Room temperature Mössbauer spectra of $Ni_xCo_{1-x}Fe_2O_4$ and the best computer fitting (blue line –tetrahedral sites and red line – octahedral sites of Fe^{3+}). (For interpretation of the references to colour in this figure legend, the reader is referred to the Web version of this article.)

shape, the best fit with the experimental point was obtained by considering two prevailing magnetic sextets and a small quadrupole doublet. The magnetic sextets attributed to Fe^{3+} ions in tetrahedral (A) and octahedral (B) positions are in good agreement with the structural data of $Ni_xCo_{1-x}Fe_2O_4$. The main Mössbauer parameters isomer shift (IS), quadrupole splitting (QS), hyperfine magnetic field (H_{hf}), relative areas of tetrahedral (A_T) and octahedral (A_O) sites and site assignment are presented in Table 3.

The dominant hyperfine magnetic sextets in the spectra indicate the magnetic order of samples. The doublets present in some spectra represent the superparamagnetic contribution of very small particles. The sextets with higher H_{hf} and IS are ascribed to Fe^{3+} ions from octahedral sites [28]. A slight decrease of H_{hf} from 51.01 to 49.57 T for octahedral sites and from 49.01 to 47.10 T for tetrahedral sites is in good agreement with the M_S dependence on Ni content.

The isomer shifts ranging from $\sim 0.27\text{--}0.30$ mm/s for tetrahedral and from $\sim 0.38\text{--}0.41$ mm/s for octahedral sites, does not depend on Ni content. This behavior indicates that s –electron density at the Mössbauer nucleus is not influenced by the Ni content in the analyzed samples. The IS values are characteristic for Fe^{3+} ions in a high spin state [29]. The small quadrupole splitting of both tetrahedral and octahedral sites does not depend significantly on Ni content, the cubic symmetry being conserved even after substitution of Co^{2+} by Ni^{2+} ions.

The cation distribution in spinel ferrites depends on many factors including thermal history and preparation method. The Mössbauer spectroscopy can be used to establish the cation distribution from area ratio of tetrahedral A and octahedral B sites [30]. Considering the preference of Ni^{2+} for octahedral sites, the general stoichiometric formula is calculated as $(Co_{0.25-0.25x}Fe_{0.75+0.25x})[Ni_xCo_{0.75-0.75x}Fe_{1.25-0.25x}]O_4$.

Table 3
Mössbauer fit results: isomer shift (IS), quadrupole splitting (QS), hyperfine magnetic field (H_{hf}), site assignment and relative area of tetrahedral (A_T) and octahedral (A_O) sites of $Ni_xCo_{1-x}Fe_2O_4$ NCs.

x	IS (mm/s)	QS (mm/s)	H_{hf} (T)	Site assignment	A_T (%)	A_O (%)
0.00	0.287	0.050	49.01	Tetra	42	
	0.408	–0.068	51.01	Octa		58
0.25	0.288	0.036	48.83	Tetra	44	
	0.394	–0.063	50.54	Octa		52
0.50	0.287	0.676	–	Paramagnetic		4
	0.284	0.029	48.62	Tetra	45	
	0.401	–0.067	50.10	Octa		53
	0.232	0.666	–	Paramagnetic		2
0.75	0.302	0.034	48.43	Tetra	42	
	0.393	–0.059	49.85	Octa		52
	0.143	0.581	–	Paramagnetic		6
1.00	0.267	0.051	47.10	Tetra	42	
	0.377	–0.066	49.57	Octa		54
	0.197	0.72	–	Paramagnetic		4
Errors	± 0.002	± 0.004	± 0.02		± 1	± 1

3.4. TEM analysis

The TEM images of $\text{Ni}_x\text{Co}_{1-x}\text{Fe}_2\text{O}_4/\text{SiO}_2$ NCs (Fig. 3) revealed crystalline planes over the amorphous SiO_2 background. In all NCs, the particles have uniform sized spherical shapes. For the samples annealed at 500 °C, the particles are not clearly delineated and the particles size is much lower than for samples annealed at higher temperatures. For the samples annealed at 800 and 1100 °C, a clearly delineation of spherical particles is observed. The average particles size (Table 4) decreases from 11.1 to 5.4 nm (500 °C), 13.7 to 8.3 nm (800 °C) and 33.1 to 20.1 nm (1100 °C) with the increase of Ni content, probably due to the higher surface tension of smaller size nanoparticles, which generates a driving force that increases agglomeration [25].

Thus, with increasing Ni^{2+} content, soft and friable

Table 4

The average particles size (D) of $\text{Ni}_x\text{Co}_{1-x}\text{Fe}_2\text{O}_4$ at 500, 800 and 1100 °C.

x	D (nm)		
	500	800	1100
0.00	11.1	13.7	33.1
0.25	10.2	12.4	30.4
0.50	8.1	10.9	26.9
0.75	6.9	9.2	23.7
1.00	5.4	8.3	20.1

agglomerates with very fine porous particles and irregular morphology were observed [21]. Moreover, an increase of nanoparticle size with the increase of temperature is observed. The increase of crystal growth rate can be attributed to volume expansion

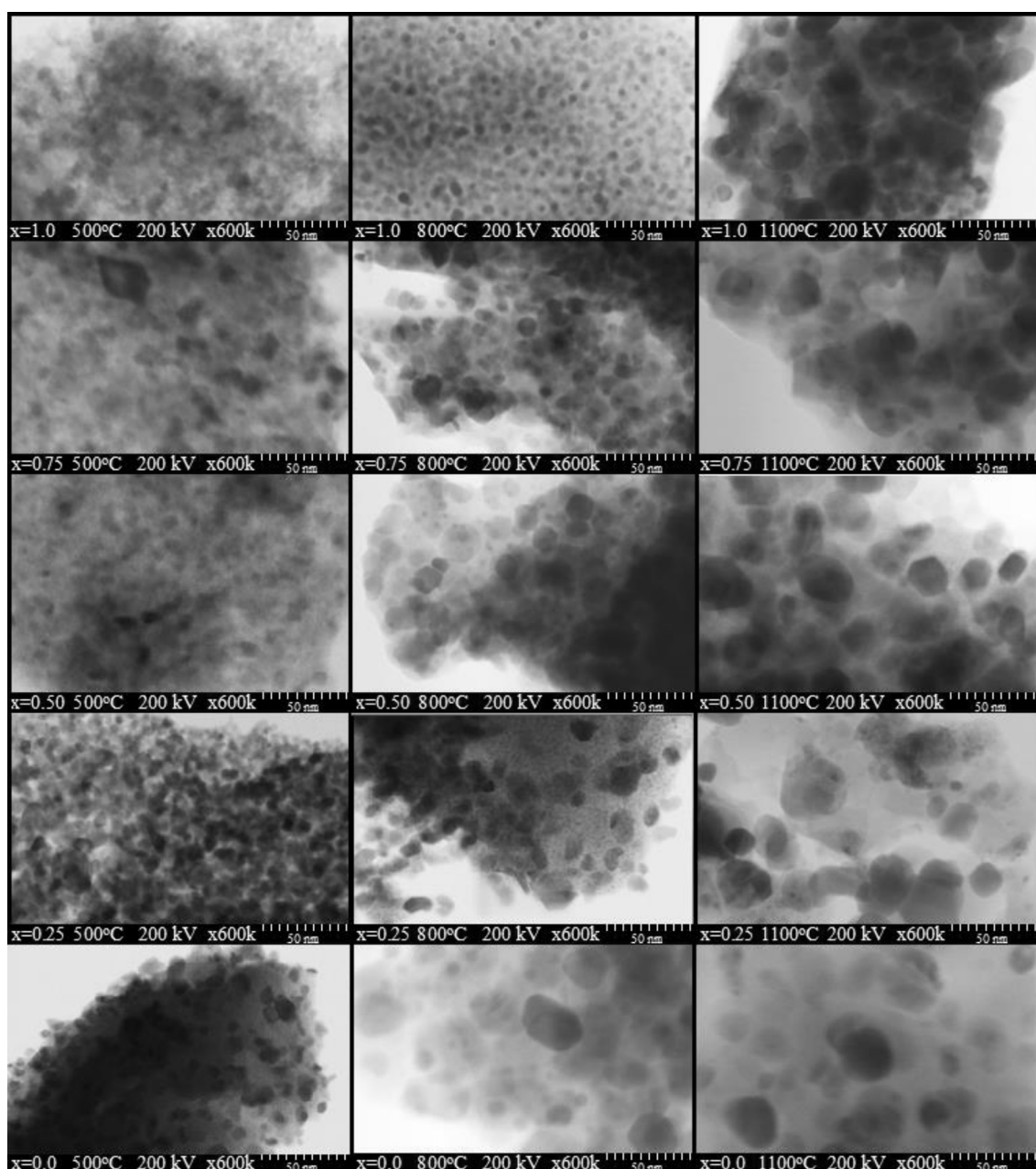


Fig. 3. TEM images of $\text{Ni}_x\text{Co}_{1-x}\text{Fe}_2\text{O}_4/\text{SiO}_2$ NCs ($x = 0-1$) annealed at 500, 800 and 1100 °C.

and supersaturation reduction of the system at high temperature (1100 °C). When the nucleation rate is higher than the growth rate, small and homogeneously distributed particles are obtained, while at high annealing temperatures, the particle size increase due to coalescence [6]. Furthermore, the high temperature increases the solubility of amorphous Fe oxides, leading to the crystallization of ferrite, as Co^{2+} and Ni^{2+} have adequate energy to diffuse into the ferrite structure [31]. The differences between the particle size obtained by XRD and TEM could be explained by the interference of amorphous SiO_2 and large-size nanoparticles that give important contribution to the diffraction patterns, as they contain a large fraction of the total number of atoms [31].

The particle size (D) distribution charts of the $\text{Ni}_x\text{Co}_{1-x}\text{Fe}_2\text{O}_4/\text{SiO}_2$ NCs ($x = 0-1$) annealed at 1100 °C are presented in Fig. 4. They were calculated from the TEM micrographs by analyzing over 100 nanoparticles for each sample. By increasing Ni content in $\text{Ni}_x\text{Co}_{1-x}\text{Fe}_2\text{O}_4/\text{SiO}_2$, the particle size decrease from 33 to 22 nm. The particle sizes estimated by XRD and TEM data are comparable.

3.5. Magnetic measurements

For the samples that didn't show saturation of magnetization in magnetic fields up to 7 T, saturation magnetization (M_s) value was obtained by fitting the $M(H)$ curve using Eq. (7) [4,20], while the magnetic moments per unit cell (n_B , in Bohr magnetons) using Eq. (8) [20]. For nano-size particles with multi-axial orientation anisotropy (K) was calculated from H_c and M_s using Eq. (9) [4,20].

$$M(H) = M_s \left(1 + \frac{a}{\mu_0 H} + \frac{b}{(\mu_0 H)^2} \right) \quad (7)$$

$$n_B = \frac{M \cdot M_s}{\mu_B \cdot N_A} \quad (8)$$

$$K = \frac{\mu_0 \cdot M_s \cdot H_c}{2} \quad (9)$$

where $M(H)$ is the magnetization, M_s is the saturation magnetization, a and b are the parameters determined by the fitting procedure, H is the magnetic field, μ_B is Bohr magneton ($9.274 \cdot 10^{-24} \text{ J/T}$), N_A is the Avogadro number, μ_0 is vacuum permeability ($\mu_0 = 1.256 \cdot 10^{-6} \text{ N/A}^2$) and H_c is the coercivity (T).

Fig. 5a shows the magnetic hysteresis loops, while Fig. 5b shows the magnetization first derivatives ($dM/d(\mu_0 H)$) with increasing Ni content in $\text{Ni}_x\text{Co}_{1-x}\text{Fe}_2\text{O}_4/\text{SiO}_2$ NCs. In almost all cases, the derivatives of the hysteresis loop exhibited small and broad peaks suggesting partially crystalline samples and the presence of large proportion of crystal defects, dislocations.

Based on hysteresis loops and $M(H)$ curves, M_s , remanent magnetization (M_r), H_c , magnetic moments per unit cell (n_B), anisotropy (K) values were determined (Table 5). The values of M_s , M_r , H_c , n_B and K decrease with increasing Ni content but they increase with the annealing temperature. In ferrites, the magnetic behavior is determined by the super-exchange interaction between the magnetic cations through oxygen atoms. The magnetic moments of the ions located in tetrahedral 'A' site and those from the octahedral 'B' site point in opposite directions [20]. The net magnetic moment is given by the difference between the two magnetizations, from A site and B. The increase of M_s and M_r values can be explained by Néel's theory and distribution of cations at tetrahedral (A) and octahedral (B) sites [2].

The spins of electrons of Fe^{3+} in A and B sites are antiparallel to each other and fail to produce a net magnetic moment of $2\mu_B$ due to Ni^{2+} ions at B sites [2]. The substituent Co^{2+} , with magnetic moment of $3\mu_B$, occupies preferably B sites. The increase in M_s and M_r originates from the replacement of Ni^{2+} ($2\mu_B$ - two unpaired electrons) with Co^{2+} ($3\mu_B$ - three unpaired electrons) that increase the number of unpaired electrons at octahedral sites [2]. The magnetic behavior of the inverse spinel (NiFe_2O_4) structure with

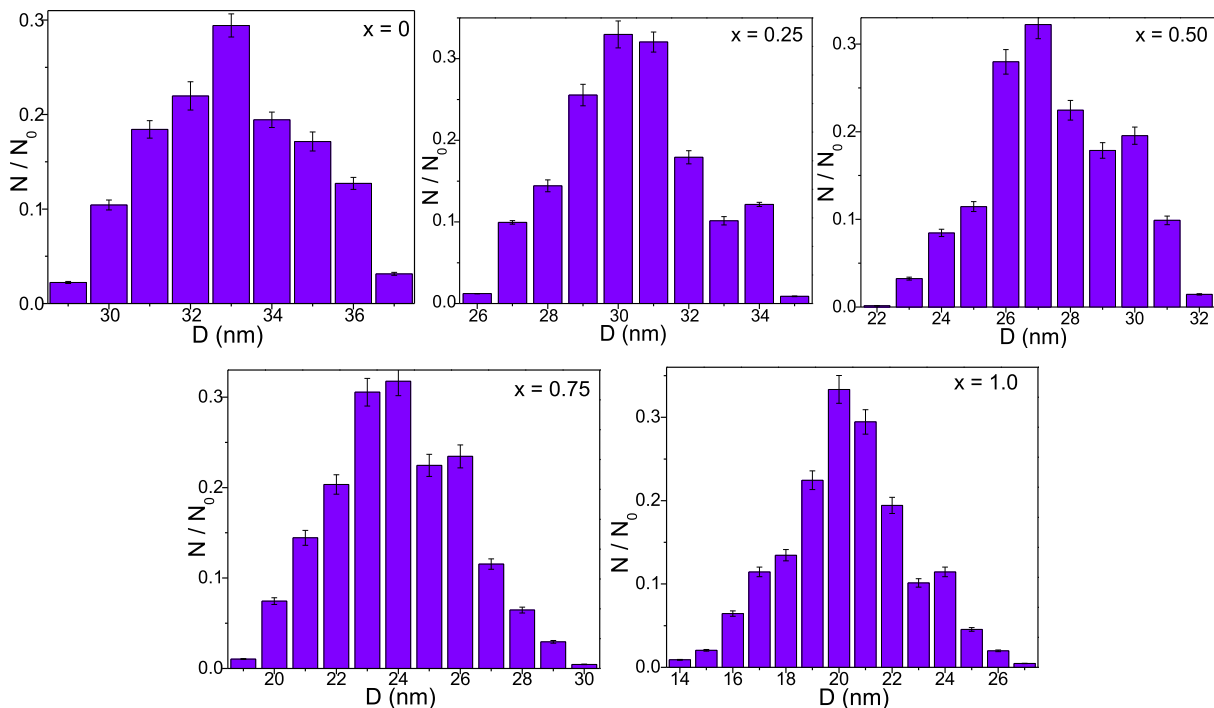


Fig. 4. Particle size distributions of $\text{Ni}_x\text{Co}_{1-x}\text{Fe}_2\text{O}_4/\text{SiO}_2$ NCs annealed at 1100 °C.

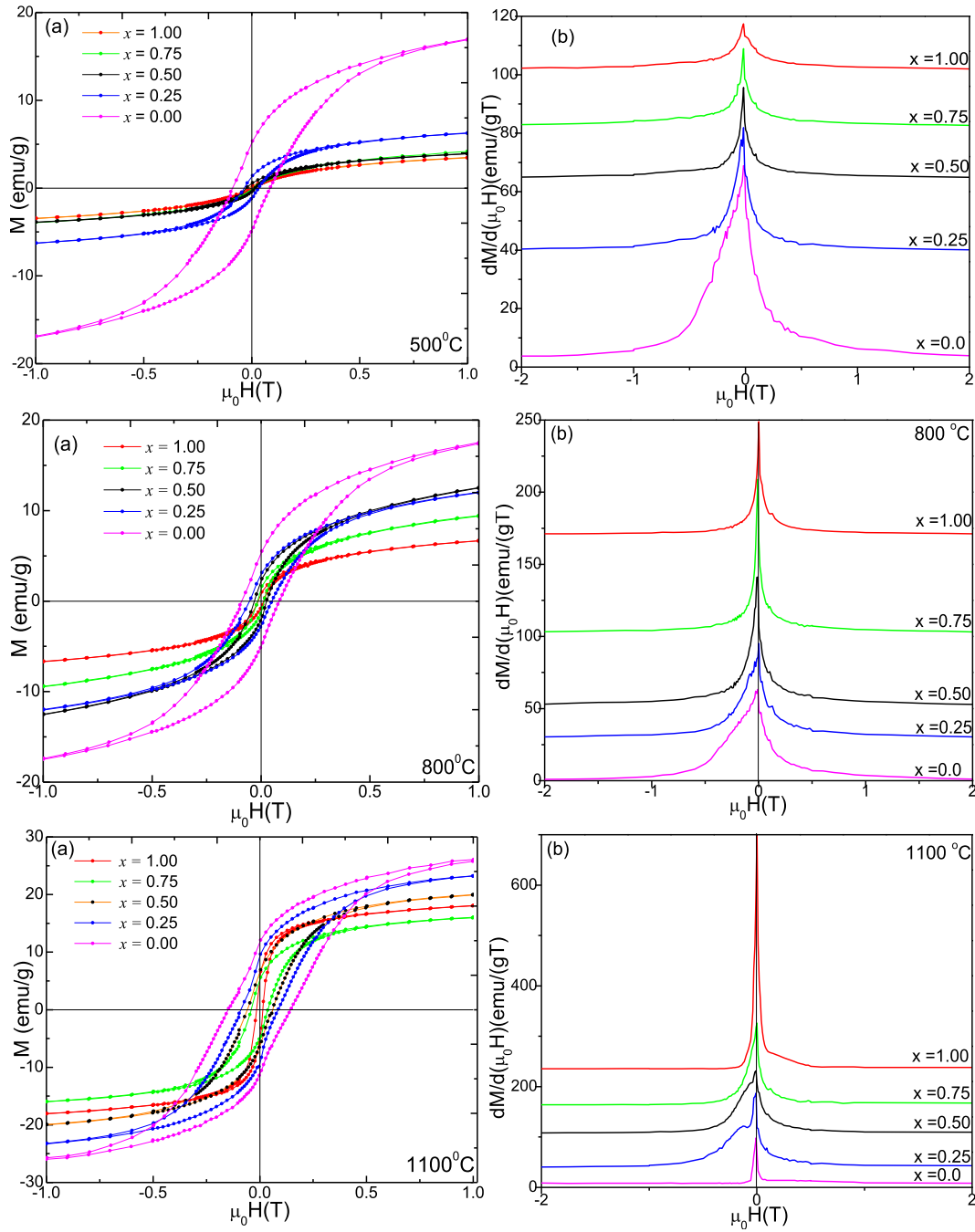


Fig. 5. Magnetic hysteresis loops (a) and magnetization derivative (b) of $Ni_xCo_{1-x}Fe_2O_4/SiO_2$ NCs annealed at 500, 800 and 1100 °C.

Table 5

Saturation magnetization (M_s), remanent magnetization (M_r), coercivity (H_c), magnetic moments per unit cell (n_B) and anisotropy (K) of $Ni_xCo_{1-x}Fe_2O_4/SiO_2$ NCs annealed at 500, 800 and 1100 °C.

x	M_s (emu/g)			M_r (emu/g)			H_c (T)			n_B			$K \cdot 10^3$ (erg/cm ³)		
	500	800	1100	500	800	1100	500	800	1100	500	800	1100	500	800	1100
0.00	22.9	23.8	29.0	5.32	5.56	12.25	0.085	0.086	0.15	0.96	1.00	1.22	1.22	1.29	2.73
0.25	9.65	18.2	25.5	1.38	3.19	9.53	0.036	0.050	0.09	0.41	0.76	1.07	0.22	0.57	1.44
0.50	7.65	17.0	22.0	0.59	2.20	6.75	0.025	0.028	0.06	0.32	0.71	0.92	0.12	0.30	0.83
0.75	7.06	15.9	19.6	0.37	1.17	5.04	0.014	0.018	0.04	0.30	0.67	0.82	0.06	0.18	0.49
1.00	6.46	11.1	19.0	0.28	0.79	4.33	0.011	0.013	0.015	0.27	0.47	0.80	0.04	0.09	0.18

formula $(NiFe)_B(Fe)_A$ is a result of the cations distribution and of the magnetization of Ni^{2+} ions that occupy octahedral sites while Co^{2+}

and Fe^{3+} ions occupy both octahedral (B) and tetrahedral (A) sites [2].

In $\text{Ni}_x\text{Co}_{1-x}\text{Fe}_2\text{O}_4$ system, the substitution ions occupy B sites. This phenomenon lowers the atomic magnetic moments, increase the saturation magnetization due to decrease of magnetic moment at that position, increase of the difference of atomic magnetic moment between A and B site and allows the A–O–B super-exchange interaction to become dominant [32].

The sample with $x = 1$, annealed at 1100°C (pure NiFe_2O_4) is completely saturated, while the other samples do not reach saturation values in the applied field range [20]. For the samples annealed at 1100°C , CoFe_2O_4 ($x = 0$) show a M_s of 29 emu/g with a magnetic moment per unit cell of $1.22\mu_B$ even at low magnetic field. The rather high magnetization value at low fields may be the result of the mixed spinel nature of nano-ferrites instead of the inverse spinel structure for cobalt-rich ferrites [20,33]. The decrease of M_s with increasing Ni content is the effect of the lower magnetic moment Ni^{2+} ($2\mu_B$), replacing the magnetic moment of Co^{2+} ($3\mu_B$) at the octahedral site [20]. This decreases M_s with increasing Ni content and decreasing crystallites size [20].

Due to the different atomic magnetic moments orientation of the metal ions, the ferromagnetism will be induced by a magnetic field [32]. The magnetic properties of Ni ferrite nanoparticles are influenced by crystallinity and particle morphology [2]. The high M_s values are determined by the presence of Co^{2+} , which have higher magnetic moment than Ni^{2+} [1]. Besides this, the Ni^{2+} substitution by Co^{2+} increases the exchanges between tetrahedral and octahedral sub-lattices, increases crystallinity and narrows particle size distribution [2]. The larger average crystallite size of CoFe_2O_4 (31.7 nm) compared to that of NiFe_2O_4 (18.2 nm) influence the super-exchange interaction and the dynamics of the magnetic domains in $\text{Ni}_x\text{Co}_{1-x}\text{Fe}_2\text{O}_4$ system [32].

The decrease of M_s with increasing Ni content result from the antiferromagnetic coupling between the magnetic moments of the ions from the neighboring A (tetrahedral) and B (octahedral) sites. The weak increase in the M_r with increasing Co content is attributed to the small remanence associated with the soft Ni-ferrites. The remanence increase is mainly due to Co^{2+} ions [2]. The presence of impurities in samples annealed at 500 and 800°C determine high magnetic disorder and reduce M_s [4].

The H_c of a magnetic material is a measure of its magnetocrystalline anisotropy [25]. For our NCs, the H_c decreases with increasing Ni content. This behavior is attributed to the larger magnetocrystalline anisotropy characteristic to CoFe_2O_4 . Since Ni substitution with Co do not show monotonous changes we can presume that Ni^{2+} ions occupy both tetrahedral and octahedral sites of the spinel structure and this cation redistribution is responsible for the magnetic changes in the ferrite particles [4]. The

low H_c suggests an enhanced coalescence of the crystallites in the nanostructures, that results in stronger magnetic coupling and higher magnetization [2]. The hysteresis loops have S-shape at low magnetic fields and linear dependence at higher fields, indicating the presence of small size magnetic particles with superparamagnetic-like behaviors [2]. The ferromagnetic behavior of the NCs containing CoFe_2O_4 as major component, with higher H_c values is revealed by the shape of the M–H curves. As Co^{2+} have higher anisotropic character than Ni^{2+} , it generates a larger H_c , when the Co content increases [2]. The increase of H_c with the Co content increase is attributed to the increase of the anisotropy field, which enhances the energy of the magnetic domain wall [2]. The materials suitable for high density recording media request higher values of M_s and H_c , provided by CoFe_2O_4 [2]. As known, CoFe_2O_4 usually forms an inverse spinel structure with very high anisotropy energy constants [25].

With increasing Ni content in $\text{Ni}_x\text{Co}_{1-x}\text{Fe}_2\text{O}_4$, the coercivity decrease together with the anisotropy decrease, lowering the value of the domain wall energy [25]. By replacing Co^{2+} by Ni^{2+} , the antiferromagnetic interaction is weakened and the ferromagnetic super-exchange interaction is enhanced, decreasing H_c and reducing M_s [25].

The variation of H_c with the Ni content and average crystallite size of $\text{Ni}_x\text{Co}_{1-x}\text{Fe}_2\text{O}_4/\text{SiO}_2$ NCs is presented in Fig. 6. The H_c rapidly decreases for $x = 0.25$, where the Co content is high, then slowly decrease with the increase of Ni content, for all annealing temperatures. Also, H_c increases with increasing crystallite size at all annealing temperatures.

A significant increase of H_c for NCs annealed at low temperature (500°C) is observed, due to magnetocrystalline anisotropy and exchange anisotropy that generates spin disorder at the surface of the particles, spin-canting, cluster-glass behavior, local chemical disorder and broken exchange interactions in the surface layers of nanoparticles [2,32,34]. For small particles, this effect is more pronounced due to the larger surface-to-volume ratio [2,18,34]. The H_c can be also increased by the enhancement of the surface potential barrier caused by the various defects in the crystalline lattice such as the deviation of atoms from the normal positions in the surface layers [2,35]. The dependence of H_c on the particle sizes considering critical size, internal strain, magnetic domain structure, shape and magnetocrystalline anisotropy of the nanoparticles is not fully elucidated [2].

The high H_c (0.015–0.15 T) values for NCs annealed at 1100°C , suggest cubic magnetic anisotropy of the ferrites and single magnetic domain structure [4]. The H_c values of NCs annealed at 500 and 800°C are lower than those of NCs annealed at 1100°C , since

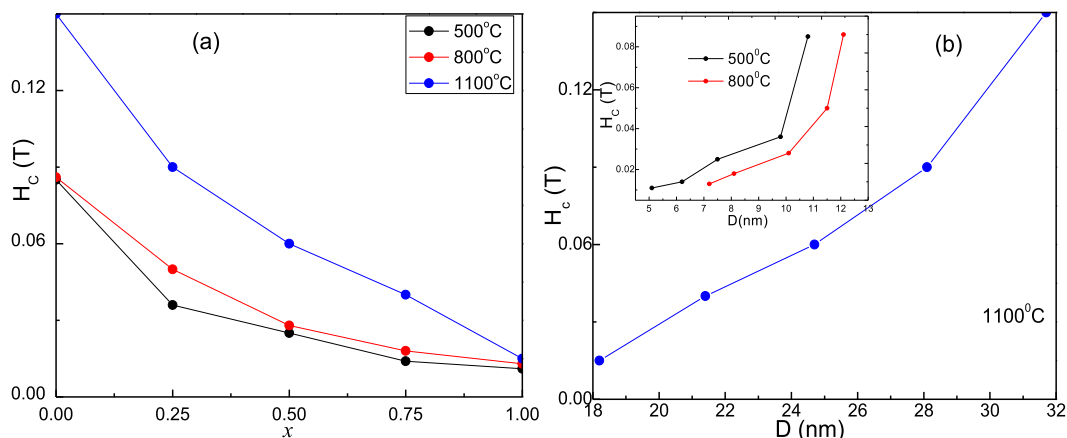


Fig. 6. Coercivity (H_c) as a function of x (a) and of average crystallite sizes, D (b), for $\text{Ni}_x\text{Co}_{1-x}\text{Fe}_2\text{O}_4/\text{SiO}_2$ annealed at 500, 800 and 1100°C .

the particle sizes increases at higher annealing temperatures. The M_r/M_s ratio is strongly related to magnetic anisotropy, particle size, shape, density, crystal defects and preparation routes [2]. The M_s decreases with decreasing the size of the nanoparticles as explained by the core shell model of the magnetic order. The values of M_s measured for Co–Ni ferrite particles also suggest that these particles have single magnetic domains with a weakly magnetized core, anti-parallel to the strongly magnetized shell [4]. The lower H_c values of NCs annealed at 500 and 800 °C suggests that H_c is not dependent on the cation redistribution but only on the Ni content of NCs.

The presence of Ni reduces the magneto crystalline anisotropy, H_c and M_s . The magnetic anisotropy is a very important parameter of a permanent magnet. The crystallographic directions, the size of the defects or the size of the inhomogeneities are responsible for the magnetic anisotropy of the sample [20].

In case of annealing at 1100 °C, NiFe_2O_4 ($K = 0.18 \cdot 10^{-3} \text{ erg/cm}^3$) has lower magnetic anisotropy than CoFe_2O_4 ($K = 2.73 \cdot 10^{-3} \text{ erg/cm}^3$). The lower values of the magnetic anisotropy of NCs annealed at 500 and 800 °C can be the consequence of the relation between the defect/inhomogeneity sizes and of the crystalline orientation [4]. The H_c of CoFe_2O_4 is much larger than that of NiFe_2O_4 . The very high anisotropy can be responsible for partial magnetic disorder in the particles. An additional contribution to the exchange anisotropy and H_c can arise from the antiferromagnetic interaction of the thin CoO shells from the surface of the nanoparticles [25].

The significant reduction of magnetic moment with the particles size makes these NCs less attractive for magnetic applications. The broad peaks in magnetization derivative curves suggest wide distributions of particle sizes leading to an increased distribution of H_c 's. The broaden peaks, quasi-split in case of samples with $x = 0$, 0.25 and 0.5 annealed at 1100 °C suggest the presence of both magnetic phases (CoFe_2O_4 and NiFe_2O_4). Due to the isomorphism, in XRD, only the CoFe_2O_4 phase can be observed. For the cases where there is no horizontal shift of the peaks from the origin the distribution of H_c is uniform due to the strong coupling between nanoparticles. The sharp peaks corresponding to NCs with high NiFe_2O_4 content suggest higher magnetic purity.

4. Conclusions

The polycrystalline $\text{Ni}_x\text{Co}_{1-x}\text{Fe}_2\text{O}_4$ ($x = 0-1$) cubic spinel, prepared by sol-gel method, displays excellent purity, crystallinity and reproducibility after annealing at 1100 °C. In this case, XRD results indicated a decrease of lattice constant (8.4379–8.3178 Å), average crystallite size (31.7–18.2 nm), unit cell volume ($600-576 \text{ Å}^3$) and hopping length in A (3.654–3.602 Å) and B (2.983–2.941 Å) sites and an increase of X-ray density (5.188–5.411 g/cm^3) and relative crystallinity (81.6–100 a. u.) with the increase of Ni content. A possible explanation could be the larger ionic radius of Co^{2+} compared to that of Ni^{2+} . According to TEM, the sizes of spherical nanoparticles decrease from 11.1 to 5.4 nm (500 °C), 13.7 to 8.3 nm (800 °C) and 33.1 to 20.1 nm (1100 °C) with the increase of Ni content, reflecting the high crystallinity at high temperatures. The Mössbauer measurements revealed only the presence of ferric ions in high spin state and established the stoichiometric formula of samples. The magnetic properties such as saturation magnetization, remanent magnetization, coercivity, magnetic moments per unit cell and anisotropy decrease with increasing Ni content but they increase with the annealing temperature, due to the influence of cation stoichiometry and their specific sites occupancy. At all annealing temperatures, CoFe_2O_4 ($x = 0$) exhibits ferromagnetic behavior, magnified hysteresis loops and enhanced magnetic properties, while NiFe_2O_4 ($x = 1$) with S-shape hysteresis loops and poor magnetic properties displays superparamagnetic behavior.

Due to their magnetic characteristics, polycrystalline Ni–Co ferrites could be used both as soft and hard magnetic materials in technical applications.

Acknowledgement

This work was supported by Sectorial Operational Program “Increase of Economic Competitiveness” Priority Axis II, Project Number 1887, INOVA-OPTIMA, code SMIS-CSNR 49164. O. Cadar acknowledges the support of a mobility grant of the Romanian Ministry of Research and Innovation, CNCS - UEFISCDI, project number PN-III-P1-1.1-MC-2018-0816, within PNCDI III. I.G. Deac acknowledges the support of the CNCS - UEFISCDI Romania, grant PN-III-P4-ID-PCE- 2016-0534 and PN-III-P4-ID-PCCF-2016-0112. Also, the authors would like to express their gratitude to Hani El Nagggar and Dr. Razvan Hirian for the magnetic measurements. One of the authors (L.D.) greatly acknowledges the financial support under the Core Program PN10N.

References

- [1] A. Singh, J. Singh, H.S. Dosanjh, Synthesis of pure and mixed Nickel-Cobalt ferrites ($\text{Ni}_{1-x}\text{Co}_x\text{Fe}_2\text{O}_4$) by combustion method and characterization, *J. Chem. Pharmaceut. Res.* 7 (2015) 612–617.
- [2] M.A. Ati, Z. Othaman, A. Samavati, Influence of cobalt on structural and magnetic properties of nickel ferrite nanoparticles, *J. Mol. Struct.* 1052 (2013) 177–182.
- [3] K. Pubby, S.S. Meena, S.M. Yusuf, S.B. Narang, Cobalt substituted nickel ferrites via Pechini's sol-gel citrate route: X-band electromagnetic characterization, *J. Magn. Mater.* 466 (2018) 430–445.
- [4] U.B. Sontu, N. Rao V.R.M. Reddy, Temperature dependent and applied field strength dependent magnetic study of cobalt nickel ferrite nano particles: synthesized by an environmentally benign method, *J. Magn. Mater.* 352 (2018) 398–406.
- [5] M.A. Ati, H. Khudhair, S. Dabagh, R.M. Rosnan, A.A. Ati, Synthesis and characterization of cobalt doped nickel - ferrites nanocrystalline by coprecipitation method, *Int. J. Sci. Eng. Res.* 5 (2014) 927–930.
- [6] K. Maaz, G.-H. Kim, Single domain limit for $\text{Ni}_x\text{Co}_{1-x}\text{Fe}_2\text{O}_4$ ($0 \leq x \leq 1$) nanoparticles synthesized by coprecipitation route, *Mater. Chem. Phys.* 137 (2012) 359–364.
- [7] P.P. Hankare, K.R. Sanadi, R.S. Pandav, N.M. Patil, K.M. Garadkar, I.S. Mulla, Structural, electrical and magnetic properties of cadmium substituted copper ferrite by sol-gel method, *J. Alloy. Comp.* 540 (2012) 290–296.
- [8] A. Gaffour, D. Ravinder, Characterization of nano-structured nickel-cobalt ferrites synthesized by citrate-gel auto combustion method, *Int. J. Sci. Eng. Res.* 4 (2014) 73–79.
- [9] S. Joshi, V.B. Kamble, M. Kumar, A.M. Umarji, G. Srivastava, Nickel substitution induced effects on gas sensing properties of cobalt ferrite nanoparticles, *J. Alloy. Comp.* 654 (2016) 460–466.
- [10] S. Torkian, A. Ghasemi, R.S. Razavi, Cation distribution and magnetic analysis of wideband microwave absorptive $\text{Co}_x\text{Ni}_{1-x}\text{Fe}_2\text{O}_4$ ferrites, *Ceram. Int.* 43 (2017) 6987–6995.
- [11] B. Rajesh Babu, M.S.R. Prasad, K.V. Ramesh, Role of synthesis on physical properties of $\text{Ni}_{0.5}\text{Zn}_{0.5}\text{Fe}_2\text{O}_4$ nanoferrite: a comparative study, *J. Supercond. Nov. Magnetism* 30 (2017) 1609–1617.
- [12] W.-O. Choi, J.-G. Lee, B.-S. Kang, K.P. Chae, Crystallographic and magnetic properties of nano-sized nickel substituted cobalt ferrites synthesized by the sol-gel method, *J. Magn.* 19 (2014) 50–63.
- [13] B. Ndlovu, J.M. Msomi, T. Moyo, Mossbauer and electrical studies of $\text{Ni}_x\text{Co}_{1-x}\text{Fe}_2\text{O}_4$ nanoparticles, *J. Alloy. Comp.* 745 (2018) 187–195.
- [14] S.U. Bhasker, G.S.V.R.K. Choudary, M.V. Ramana Reddy, Modulation in magnetic exchange interaction, core shell structure and Hopkinson's peak with chromium substitution into $\text{Ni}_{0.75}\text{Co}_{0.25}\text{Fe}_2\text{O}_4$ nano particles, *J. Magn. Mater.* 454 (2018) 349–355.
- [15] A. Ramakrishna, N. Murali, S.J. Margarete, K. Samatha, V. Veeraiah, Comparative study of synthesis, structural and magnetic properties of Cu^{2+} substituted Co-Ni, Co-Zn and Co-Mg nano ferrites, *Phys. B Condens. Matter* 530 (2018) 251–257.
- [16] M.K. Kokare, N.A. Jadhav, Vijay Singh, S.M. Rathod, Effect of Sm^{3+} substitution on the structural and magnetic properties of Ni-Co nanoferrites, *Optic Laser. Technol.* 112 (2019) 107–116.
- [17] A.H. Morrish, *The Physical Principles of Magnetism*, Wiley, New York, 1965, p. 394.
- [18] Joint Committee on Powder Diffraction Standards- International Center for Diffraction Data, 1999.
- [19] T. Prabhakaran, J. Hemalatha, Combustion synthesis and characterization of cobalt ferrite nanoparticles, *Ceram. Int.* 42 (2016) 14113–14120.
- [20] U.B. Sontu, V. Yelasani, V.R.R. Musugu, Structural, electrical and magnetic

- characteristics of nickel substituted cobalt ferrite nanoparticles, synthesized by self combustion method, *J. Magn. Magn Mater.* 374 (2015) 376–380.
- [21] M. Roberto de Freitas, G. Lisboa de Gouveia, L.J. Dalla Costa, A.J. Aparecido de Oliveira, R.H.G.A. Kiminami, Microwave assisted combustion synthesis and characterization of nanocrystalline nickel-doped cobalt ferrites, *Mater. Res.* 19 (2016) 27–32.
- [22] T. Dippong, E.A. Levei, O. Cadar, A. Mesaros, G. Borodi, Sol-gel synthesis of $\text{CoFe}_2\text{O}_4/\text{SiO}_2$ nanocomposites - insights into the thermal decomposition process of precursors, *J. Anal. Appl. Pyrol.* 125 (2017) 169–177.
- [23] P.P. Hankare, K.R. Sanadi, K.M. Garadkar, D.R. Patil, I.S. Mulla, Synthesis and characterization of nickel substituted cobalt ferrite nanoparticles by sol-gel auto-combustion method, *J. Alloy. Comp.* 553 (2013) 383–388.
- [24] K. Maaz, S. Karim, A. Mashiatullah, J. Liu, M.D. Hou, Y.M. Sun, J.L. Duan, H.J. Yao, D. Mo, Y.F. Chen, Structural analysis of nickel doped cobalt ferrite nanoparticles prepared by coprecipitation route, *Physica B* 404 (2009) 3947–3951.
- [25] A. Baykal, N. Kasapoglu, Y. Koseoglu, A.C. Basaran, H. Kavas, M.S. Toprak, Microwave-induced combustion synthesis and characterization of $\text{Ni}_x\text{Co}_{1-x}\text{Fe}_2\text{O}_4$ nanocrystals ($x = 0.0, 0.4, 0.6, 0.8, 1.0$), *Cent. Eur. J. Chem.* 6 (2018) 125–130.
- [26] T. Dippong, E.A. Levei, O. Cadar, F. Goga, G. Borodi, L. Barbu-Tudoran, Thermal behavior of $\text{Co}_x\text{Fe}_{3-x}\text{O}_4/\text{SiO}_2$ nanocomposites obtained by a modified sol-gel method, *J. Therm. Anal. Calorim.* 128 (2017) 39–52.
- [27] T. Dippong, O. Cadar, E.A. Levei, C. Leostean, L. Barbu Tudoran, Effect of annealing on the structure and magnetic properties of $\text{CoFe}_2\text{O}_4/\text{SiO}_2$ nanocomposites, *Ceram. Int.* 43 (2017) 9145–9152.
- [28] A. Lakshman, P.S.V. Subba Rao, K.H. Rao, Mössbauer spectroscopic analyses of $\text{Mg}_{0.9}\text{Cu}_{0.1}\text{Mn}_{0.05}\text{Cr}_x\text{Fe}_{1.95-x}\text{O}_4$ spinel ferrites, *Mater. Lett.* 60 (2006) 7–10.
- [29] N.N. Greenwood, T.C. Gibb, *Mössbauer Spectroscopy*, Chapman and Hall Ltd., London, 1971.
- [30] D. Gingașu, I. Mîndru, S. Preda, J.M. Calderon-Moreno, D.C. Culiță, L. Patron, L. Diamandescu, Green synthesis of cobalt ferrite nanoparticles using plant extracts, *Rev. Roum. Chim.* 62 (2017) 645–653.
- [31] L. Rednic, I.G. Deac, E. Dorolti, M. Coldea, V. Rednic, M. Neumann, Magnetic cluster development in $\text{In}_{1-x}\text{Mn}_x\text{Sb}$ semiconductor alloys, *Cent. Eur. J. Phys.* 8 (2010) 620–627.
- [32] G. Xi, Y. Xi, Effects on magnetic properties of different metal ions substitution cobalt ferrites synthesis by sol-gel auto-combustion route using used batteries, *Mater. Lett.* 164 (2016) 444–448.
- [33] K.M. Batoo, M.-S. Abd El-Sadek, Electrical and magnetic transport properties of Ni–Cu–Mg ferrite nanoparticles prepared by sol-gel method, *J. Alloy. Comp.* 566 (2013) 112–119.
- [34] T. Dippong, O. Cadar, E.A. Levei, I. Bibicu, L. Diamandescu, C. Leostean, M. Lazar, G. Borodi, L. Barbu-Tudoran, Structure and magnetic properties of $\text{CoFe}_2\text{O}_4/\text{SiO}_2$ nanocomposites obtained by sol-gel and post annealing pathways, *Ceram. Int.* 43 (2017) 159–177.
- [35] M. Raekers, K. Kupper, H. Hesse, I. Balasz, I.G. Deac, S. Constantinescu, E. Burzo, M. Valeanu, M. Neumann, Investigation of chemical and grain boundary effects in highly ordered SrFeMoO_6 : XPS and Mossbauer studies, *J. Optoelectron. Adv. Mater.* 8 (2006) 455–460.